Imaging Light-Induced Migration of Dislocations in Halide Perovskites with 3D Nanoscale Strain Mapping

SUPPORTING INFORMAITON

Kieran W. P. Orr[1,2], Jiecheng Diao[†3], Muhammad Naufal Lintangpradipto[4], Darren J. Batey[5], Affan N. Iqbal[1,2], Simon Kahmann[1,2], Kyle Frohna[1,2], Milos Dubajic[1], Szymon J. Zelewski[1,2], Alice E. Dearle[1,2,6], Thomas A. Selby[1], Peng Li[5], Tiarnan A. S. Doherty[1,2,7], Stephan Hofmann[6], Osman M. Bakr[4], Ian K. Robinson[3,8], Samuel D. Stranks*[1,2]

---

[1]*Department of Chemical Engineering and Biotechnology, University of Cambridge, Philippa Fawcett Drive, Cambridge, CB3 0AS, UK*

[2]*Department of Physics, Cavendish Laboratory, University of Cambridge, JJ Thomson Avenue, Cambridge, CB3 0HE, UK*

[3]*London Centre for Nanotechnology, University College London, London WC1E 6BT, UK*

[4]*Physical Science and Engineering (PSE) Division, King Abdullah University of Science and Technology (KAUST) Thuwal 23955-6900, Kingdom of Saudi Arabia*

[5]*Diamond Light Source, Harwell Science and Innovation Campus, Fermi Ave, Didcot OX11 0DE, UK*

[6]*Department of Engineering, University of Cambridge, UK*

[7]*Department of Materials Science & Metallurgy, University of Cambridge, 27 Charles Babbage Road, Cambridge, CB3 0FS, United Kingdom*

[8]*Condensed Matter Physics and Materials Science Department, Brookhaven National Lab, Upton, New York 11793, USA*

*sds65@cam.ac.uk

[†]Current address: *Center for Transformative Science, ShanghaiTech University, Shanghai 201210, China*.

SUPPORTING NOTE 1:

Additional information regarding BCDI reconstructions:

The validity of a given reconstruction can be assessed by considering its χ^2 value, which is defined as follows.

$$\chi^2 = \frac{\sum_i \left||A_\mathrm{r}(\mathbf{q}_i)|^2 - |A_\mathrm{m}(\mathbf{q}_i)|^2\right|}{\sum_i |A_\mathrm{m}(\mathbf{q}_i)|^2}$$

Here, $A_\mathrm{r}(\mathbf{q}_i)$ and $A_\mathrm{m}(\mathbf{q}_i)$ are the amplitudes of the diffraction pattern from the reconstruction and the measurement respectively, with i counting over all pixels on the X-ray detector. The diffracted intensity, $I(\mathbf{q}_i) = |A(\mathbf{q}_i)|^2$. $\mathbf{q}$ is a position vector in reciprocal space. A small value of χ^2 therefore implies that the reconstruction's diffraction pattern is very similar to the measured diffraction pattern and that the reconstruction is an accurate representation of the diffracting crystal in real space.

χ^2 values for all reconstructions presented in this work are given in Supporting Table S1 below. The values are small so we can be confident in our reconstructions. We note that the χ^2 values for the crystals that have suffered beam damage are higher than the others, most likely because the X-ray beam causes changes to the crystal structure during the measurement.

Additionally, reconstructions were performed multiple times with random initial starting guesses of diffraction pattern phases and real-space support volume and were checked for consistency. Example error metrics for the reconstruction shown in Figure 2a of the main text and Figure S2a, starting with different random guesses for the diffraction pattern phases and reconstruction electron density, are shown in Supporting Table S2. The χ^2 values for reconstructions arising different initial electron density guesses and initial diffraction pattern phase guesses converge, showing that the reconstruction process is robust and reliable.

Similar nanoscale strain and orientational information could be obtained using electron microscopy techniques such as atomic resolution scanning transmission electron microscopy (STEM), electron backscatter diffraction (EBSD), and/or electron tomography. Data from BCDI could be compared with data from these techniques to check for consistency. However, as mentioned in the main text, due to the high sensitivity of halide perovskites to electron beams, carrying out such measurements would be very challenging and beyond the scope of this work.

The diffraction patterns that were reconstructed in this work are of high quality with background pixels having counts of 1-2 counts, and maximum intensity pixels have *ca.* 5000 counts, giving us excellent signal/noise ratios. In order to successfully reconstruct a crystal in real space, one must satisfy the "oversampling condition" such that at least double the number of data points are recorded in reciprocal space as there are values of real space electron density to be computed. Further, the spacing of atomic fringes (π divided by the size of the object in real space) must be larger than the detector pixel size, otherwise fringes cannot be properly resolved. In practice, this means placing the detector far away from the sample, so the fringes have time to spread out. If any of these conditions are not met, or if counting statistics are poor in the collected diffraction patterns, then the reconstructions will become obviously noisy (with very rough iso-surfaces, for example).

For more details on the BCDI technique, we refer the reader references [1-4].

SUPPORTING NOTE 2:

Missing reconstruction volume due to crystal structure twisting:

Where reconstructions are not well faceted, the missing volume is due to parts of the crystal that do not satisfy the Bragg condition for the position of the detector at the beamline. For example, such regions of a crystal could be twisted into another orientation. We find evidence for such twisting in related $MAPbBr_3$ crystals which are large and flat, and are synthesised in an analogous fashion to the crystals considered in the main text. Figure S1a and S1b show two maps of diffracted X-ray intensity from one of these large, flat $MAPbBr_3$ crystals. The difference in incidence angle between the sample and X-ray beam for these two maps is 0.05°. Regions (outlined in orange) of high diffracted intensity in Figure S1b align with regions of low diffracted intensity in Figure S1a indicating that these regions of the crystal must be misoriented from each other by 0.05°. This large, flat crystal of $MAPbBr_3$ is contiguous and the shape of the crystal does not give obvious reasons for the lattice misorientation within its structure (Figure S1c).

Therefore, any lack of faceting in the reconstructions shown in the main text is likely due to misalignment of the crystalline lattice towards the edges of a well-facetted crystal (Figure 1c & d of the main text confirm the well-facetted nature of our sample crystals), rather than any errors in reconstruction.

Another possible reason for any missing volumes in the reconstruction could be due to the presence of point defects and vacancies in the samples which lower the overall scattering power of the crystals, resulting in smaller reconstruction volumes.

The large flat single crystals of $MAPbBr_3$ such as the one considered here are made according to the following synthesis procedure (closely related to the procedures used to make the samples considered in the main text). A $MAPbBr_3$ precursor solution of methylammonium bromide (Great Cell Solar, >99.99%) and lead (II) bromide (TCI, >98.0%) in N,N-dimethylformamide (Sigma-Aldrich, 99.8%) was prepared with concentration 1 M. A droplet of very limited volume (<< 1µL) of MAPbBr3 precursor solution, was deposited onto a silicon wafer coated in 10 µm of SiO_2. The precursor droplet is rapidly confined with an exfoliated flake of biotite mica. After *ca.* 72 hours; space-confined perovskite crystallisation occurs by evaporation and the biotite mica flake can be easily removed.

SUPPORTING NOTE 3:

Control scans for crystal in Figure 3 of the main text in dark conditions:

In order to confirm that dislocations migrate more easily under visible light illumination, we first needed to collect BCDI data in dark conditions (*i.e.* with only the beamline hutch ambient lights on). For the crystal considered in Figure 3 of the main text, we first measured four BCDI scans without laser illumination. These reconstructions are shown in Figure S2. The overall shape of the reconstruction is largely reproducible and the dislocation remains along the long-axis of the reconstruction (also see Supporting Video 1). Under illumination the dislocations become highly mobile, as shown in Figure 3 of the main text.

Further, we can be confident the increased dislocation migration is caused by the visible light illumination, as opposed to X-ray beam damage, because the crystal is radiation stable as confirmed by the plots of Bragg peak intensity as a function of rocking curve angle for successive scans shown in Figure S3. We can also be confident that the crystals are not being damaged by the X-ray beam because the region of sample that was exposed to the X-ray beam for the scans leading to the reconstructions in Figure 3 of the main text shows no difference in PL spectrum compared to a nearby region of sample that was not exposed to the beam as is shown in Figure S4.

It is possible that the crystal undergoes damage on a very fast timescale when the X-ray beam is first incident on the sample. However, this is unlikely given the crystal's subsequent stability. In any case, we see dramatically faster changes in the internal strain fields of the crystal under visible illumination *vs.* dark conditions, regardless of whether the crystal suffered any damage at an earlier time.

A beam energy of 11.8 keV was used for the BCDI scans for Figure 3. This X-ray energy was far less damaging than 9.7 keV which was used for the measurements where we saw definite beam damage (Figure 4 of the main text and Figure S23).

SUPPORTING TABLE S1:

Where does the reconstruction appear?	Fraction of crystal volume with local strain greater than 1%, f /%	Root mean squared local strain, $\epsilon_{\mathbf{rms}}$ /%	χ^2
Main text Figure 1b	13.2	0.7	0.054
Main text Figure 2a & Figure S2a	18.7	2.9	0.088
Figure S2b	23.6	3.1	0.084
Figure S2c	27.1	4.3	0.071
Main text Figure 3a & Figure S2d	27.9	3.9	0.085
Main text Figure 3b	14.9	3.6	0.091
Main text Figure 3c	25.0	3.6	0.091
Main text Figure 3d	23.0	3.8	0.076
Main text Figure 3e	21.2	3.5	0.087
Main text Figure 4a & 4b	13.2	1.0	0.084
Main text Figure 4c & 4d (beam damaged)	48.0	5.1	0.139
Figure S24a & S24b	6.6	0.6	0.052
Figure S24c & S24d (beam damaged)	14.2	1.9	0.135

Table S1: Local strain in $MAPbBr_3$ microcrystals: By taking the spatial derivative of the atomic displacement field between voxels of the reconstructions with respect to the X-ray scattering vector direction we calculate the local nanoscale tensile (positive)/compressive (negative) strain in a crystal. These values can be plotted as a histogram, such as the one shown in Figure 1e of the main text. We then calculate the fraction of points where the local tensile/compressive strain is greater than 1% (shown by the orange regions of the histogram in Figure 1e of the main text). We also tabulate the root mean square local strain within the crystals. χ^2 values for each reconstruction are shown in the final column (see Supporting Note 1).

Histograms of the underlying local strain distributions are shown at the end of the Supporting Figures (apart from that for the crystal in Figure 1b of the main text which is shown in Figure 1e of the main text).

SUPPORTING TABLE S2:

Starting guess	χ^2
Random electron density guess 1	0.088
Random electron density guess 2	0.088
Random electron density guess 3	0.088
Random phases guess 1	0.085
Random phases guess 2	0.085
Random phases guess 3	0.085

Table S2: χ^2 error metrics for reconstructions starting from different initial starting guesses: Each reconstruction presented in this work was reconstructed from its respective diffraction pattern multiple times with different starting guesses for the electron density and diffraction pattern phases. The χ^2 values for each of six resulting reconstructions for the one shown in Figure 2a of the main text and Figure S2a are shown. These are representative of the values obtained for the other reconstructions.

SUPPORTING FIGURES:

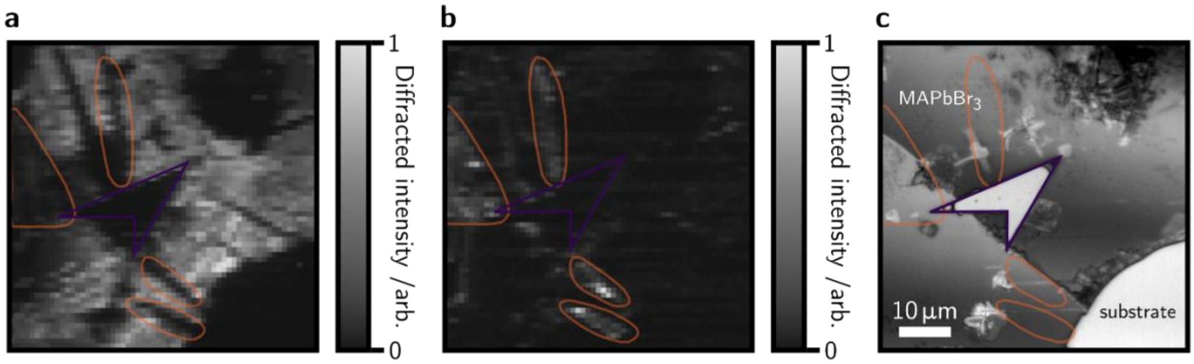

Figure S1: Misorientation within a MAPbBr$_3$ single crystal: a and **b** show maps of diffracted intensity as the X-ray beam is raster scanned across the sample. The difference in rocking angle at which the sample was held for scan **a** and **b** is 0.05°. **c** shows a broadband optical microscopy image of this same region of crystal (as can be identified by the arrow-head shape highlighted in purple).

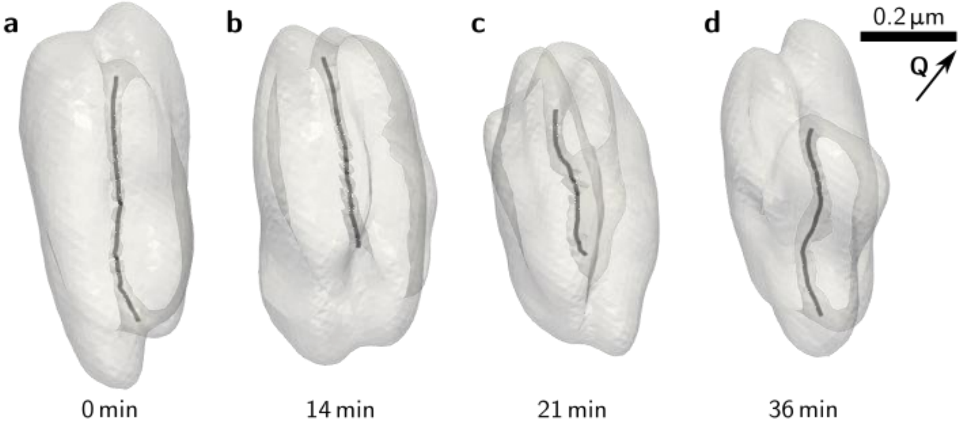

Figure S2: Control reconstructions for crystal considered in Figure 3 of the main text: Reconstructions of successive BCDI scans for the crystal considered in Figure 3 of the main text. Four scans were carried out on the crystal before illuminating with the 405 nm laser to check that the crystal was stable to the X-ray radiation. **a**, **b**, **c**, and **d** show the reconstructions from these scans with the dislocation highlighted in black. The time given under the reconstruction is the time of the scans relative to the first (**a**). The scale bar and scattering vector apply to all reconstructions. The reconstruction shown in panel **d** is the same as that shown in Figure 3a of the main text. Burgers vector characterisation for the dislocations in these crystals confirming that they are all ⟨100⟩ edge dislocations are shown in Figures S5-S8.

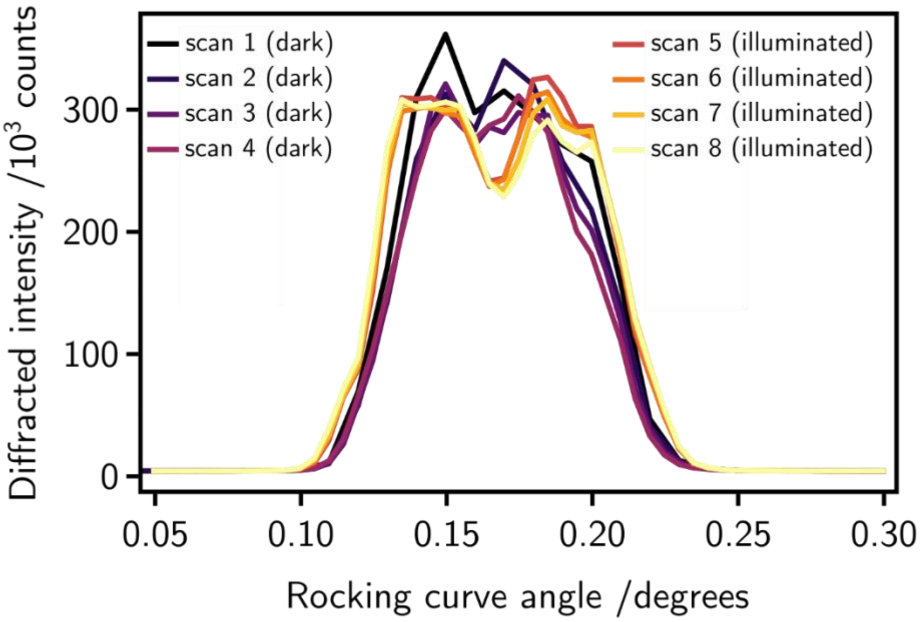

Figure S3: Radiation stability of crystal considered in Figures S2 and S3 of the main text: Bragg peak intensity as a function of rocking curve angle for successive scans of the MAPbBr$_3$ microcrystal considered in Figure S2 and Figure S3 of the main text. The Bragg peak intensity and general shape is constant, indicating negligible beam damage is taking place during each successive scan for this crystal.

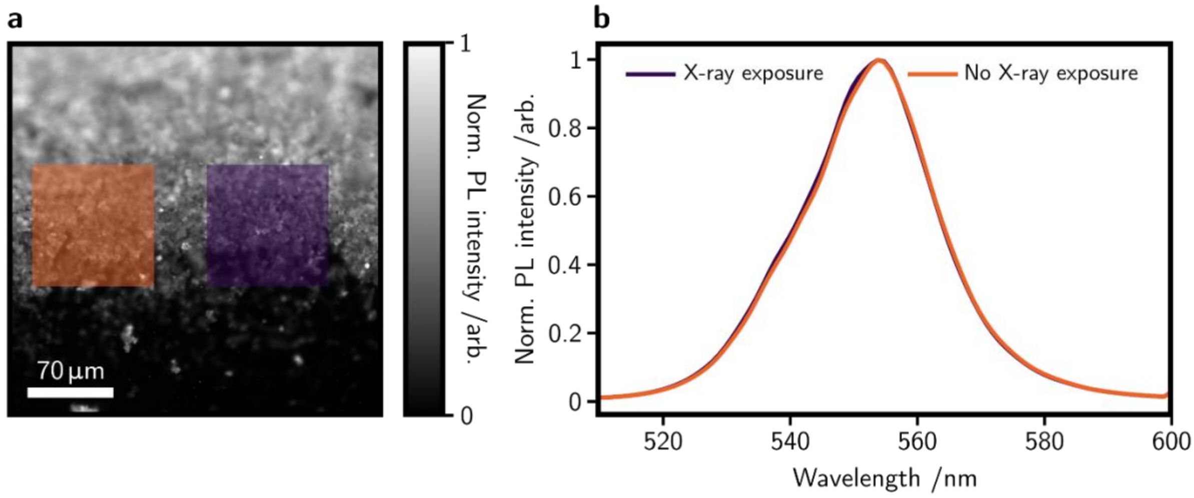

Figure S4: PL stability of crystals under 11.8keV X-rays: a Map of normalised PL emission intensity of a microcrystal film. The black region at the bottom of the image is where the film ends and the top of the image is out of focus because the edge of the film thins gradually rather than abruptly. The centre of the image is in focus at a mid-point of the microcrystal film thickness. The region highlighted in purple was exposed to X-rays and the region highlighted in orange was not. **b** PL emission spectra from the purple and orange regions in **a**. No significant differences in PL emission spectra are observed, further confirming lack of beam damage.

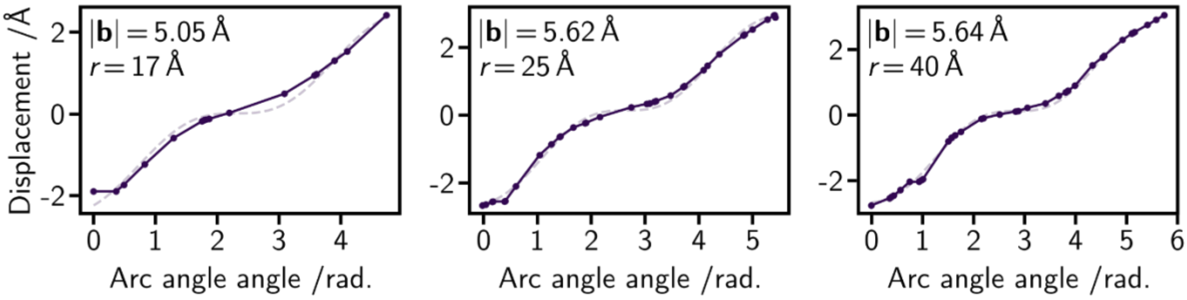

Figure S5: Burgers vector calculation for Figure S2a (dark): Atomic displacements as a function of arc angle as we circle the dislocation core at three different radii. Dashed lines: fit to data of function for atomic displacement, u, given in the main text. Average Burgers vector magnitude is 5.44Å.

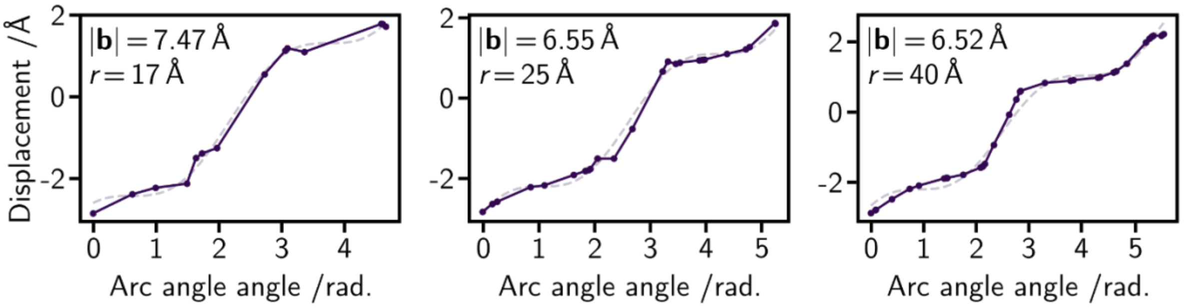

Figure S6: Burgers vector calculation for Figure S2b (dark): Atomic displacements as a function of arc angle as we circle the dislocation core at three different radii. Dashed lines: fit to data of function for atomic displacement, u, given in the main text. Average Burgers vector magnitude is 6.84Å.

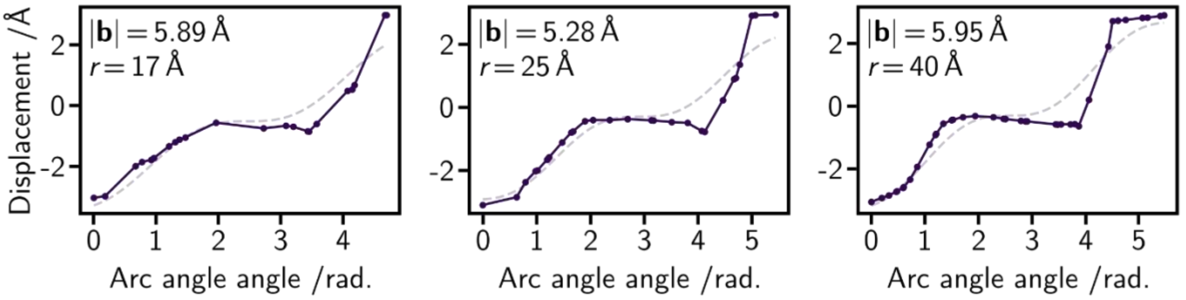

Figure S7: Burgers vector calculation for Figure S2c (dark): Atomic displacements as a function of arc angle as we circle the dislocation core at three different radii. Dashed lines: fit to data of function for atomic displacement, u, given in the main text. Average Burgers vector magnitude is 5.71Å.

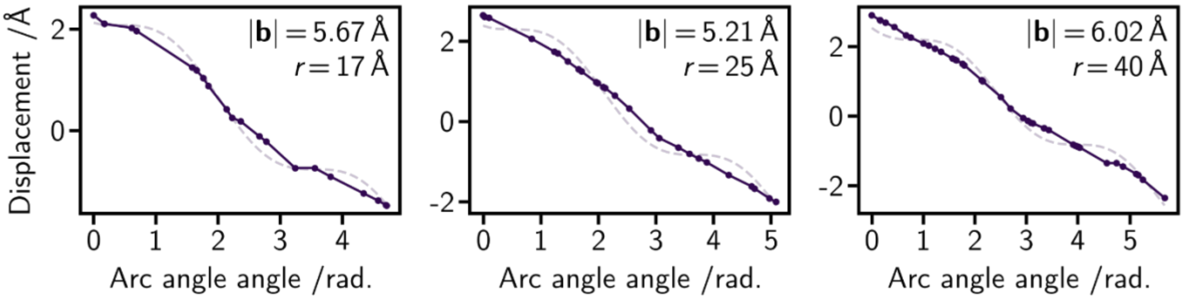

Figure S8: Burgers vector calculation for Figure 3a of the main text and Figure S2d (dark): Atomic displacements as a function of arc angle as we circle the dislocation core at three different radii. Dashed lines: fit to data of function for atomic displacement, u, given in the main text. Average Burgers vector magnitude is 5.97Å.

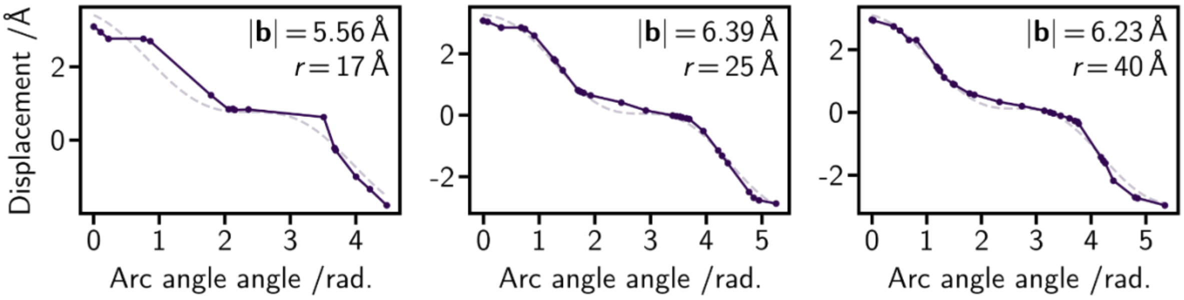

Figure S9: Burgers vector calculation for Figure 3b of the main text (illuminated): Atomic displacements as a function of arc angle as we circle the dislocation core at three different radii. Dashed lines: fit to data of function for atomic displacement, u, given in the main text. Average Burgers vector magnitude is 6.06Å. Illumination time = 0 min (after 105 min of scan parameter re-optimisation under illumination).

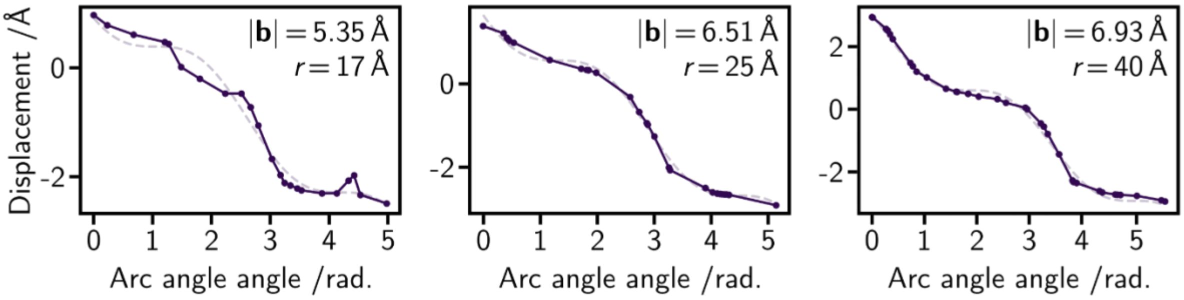

Figure S10: Burgers vector calculation for Figure 3c of the main text: Atomic displacements as a function of arc angle as we circle the dislocation core at three different radii. Dashed lines: fit to data of function for atomic displacement, u, given in the main text. Average Burgers vector magnitude is 6.26Å. Illumination time = 14 min (after 105 min of scan parameter re-optimisation under illumination).

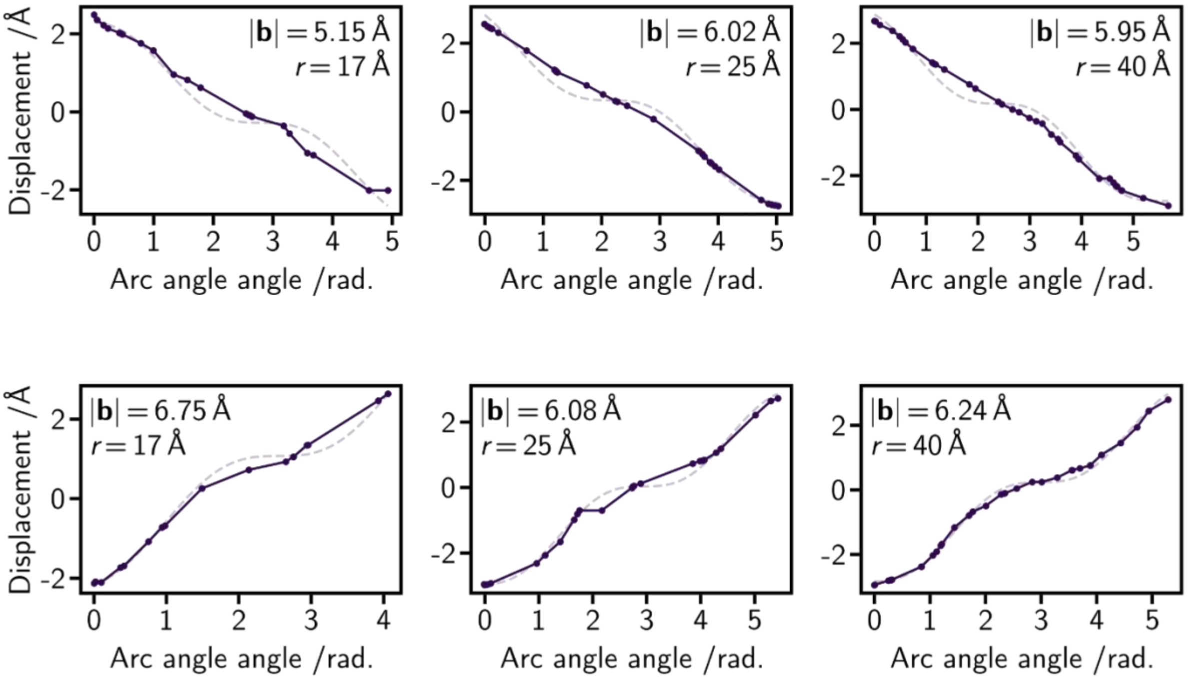

Figure S11: Burgers vector calculation for Figure 3d of the main text: Atomic displacements as a function of arc angle as we circle the dislocation core at three different radii. Dashed lines: fit to data of function for atomic displacement, u, given in the main text. Average Burgers vector magnitudes are 5.70Å (long dislocation) and 6.36Å (short dislocation). Illumination time = 27 min (after 105 min of scan parameter re-optimisation under illumination).

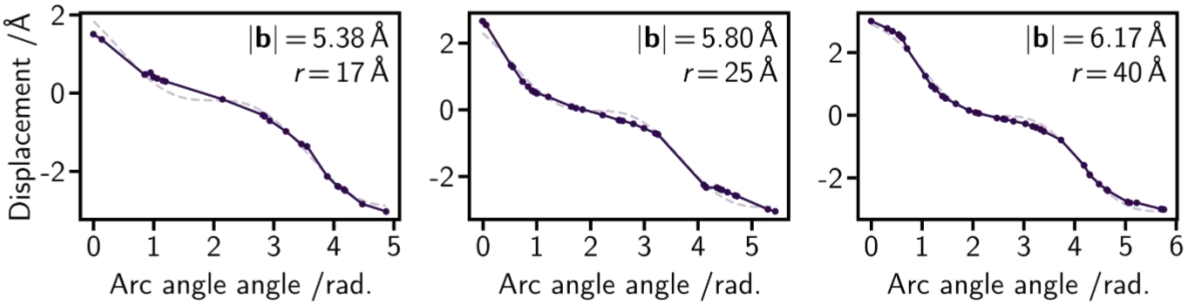

Figure S12: Burgers vector calculation for Figure 3e of the main text: Atomic displacements as a function of arc angle as we circle the dislocation core at three different radii. Dashed lines: fit to data of function for atomic displacement, u, given in the main text. Average Burgers vector magnitude is 5.78Å. Illumination time = 37 min (after 105 min of scan parameter re-optimisation under illumination).

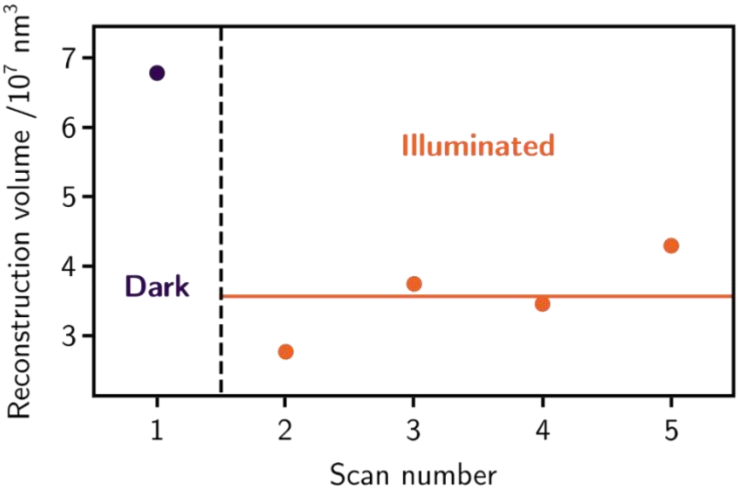

Figure S13: Volumes of reconstructions shown in Figure 3 of the main text: Values given are calculated using an isovolume threshold value of 0.16 (maximum electron density normalised to 1). The horizontal line shows the average volume for the reconstructions in when measuring under illumination.

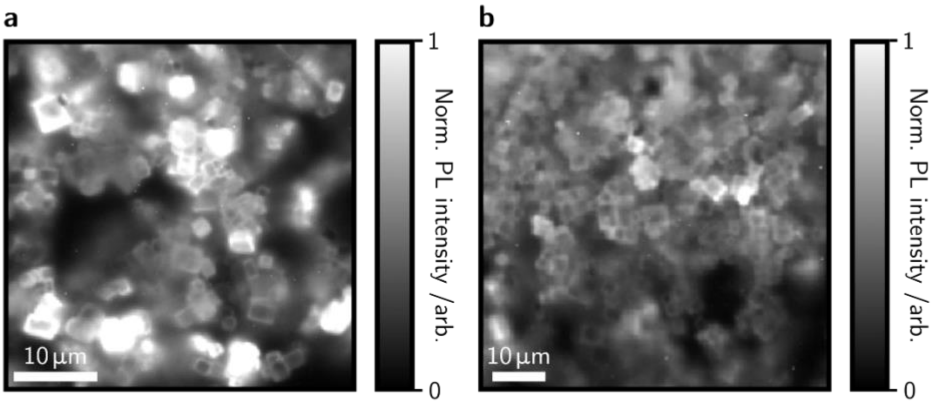

Figure S14: PL microscopy: Total emitted PL intensity images (405nm excitation wavelength) of **a** pristine $MAPbBr_3$ microcrystals, and **b** microcrystals in a region of a microcrystal film sample that was exposed to X-rays. Measurements were carried out using a hyperspectral microscope according to the method given in the main text. It can be seen that the crystals are well facetted before and after X-ray exposure.

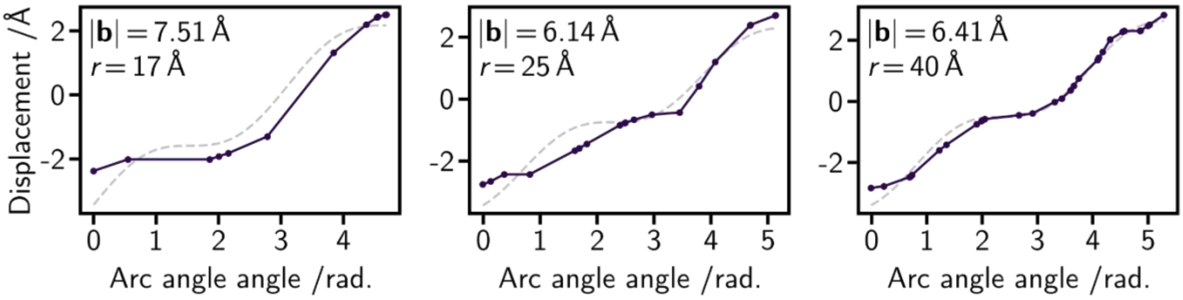

Figure S15: Burgers vector calculation for crystal in Figure 4a and b of the main text, long dislocation: Atomic displacements as a function of arc angle as we circle the dislocation core at three different radii. Dashed lines: fit to data of function for atomic displacement, u, given in the main text. Average Burgers vector magnitude is 6.69Å.

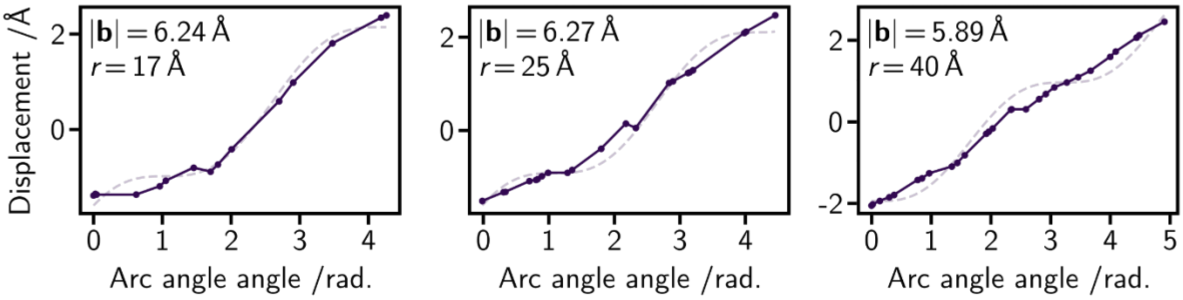

Figure S16: Burgers vector calculation for crystal in Figure 4a and b of the main text, short dislocation: Atomic displacements as a function of arc angle as we circle the dislocation core at three different radii. Dashed lines: fit to data of function for atomic displacement, u, given in the main text. Average Burgers vector magnitude is 6.13Å.

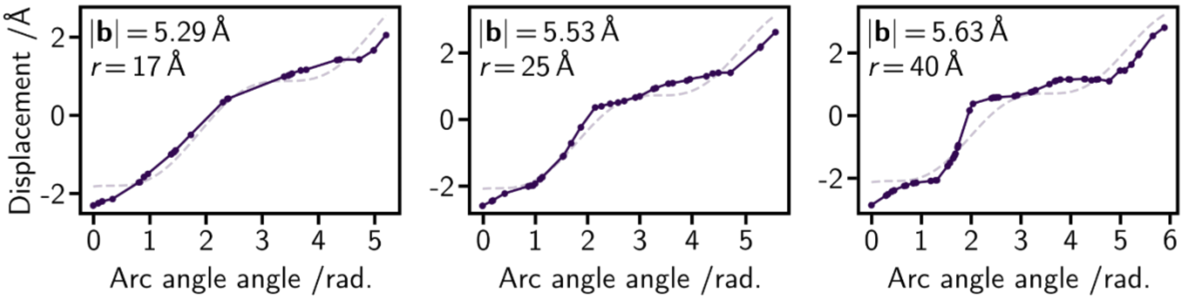

Figure S17: Burgers vector calculation for crystal in Figure 4c and d of the main text, dislocation 1: Atomic displacements as a function of arc angle as we circle the dislocation core at three different radii. Dashed lines: fit to data of function for atomic displacement, u, given in the main text. Average Burgers vector magnitude is 5.48Å.

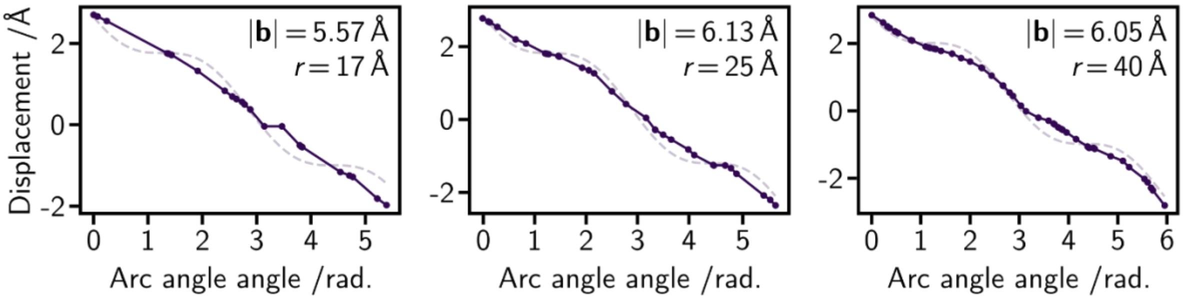

Figure S18: Burgers vector calculation for crystal in Figure 4c and d of the main text, dislocation 2: Atomic displacements as a function of arc angle as we circle the dislocation core at three different radii. Dashed lines: fit to data of function for atomic displacement, u, given in the main text. Average Burgers vector magnitude is 5.92Å.

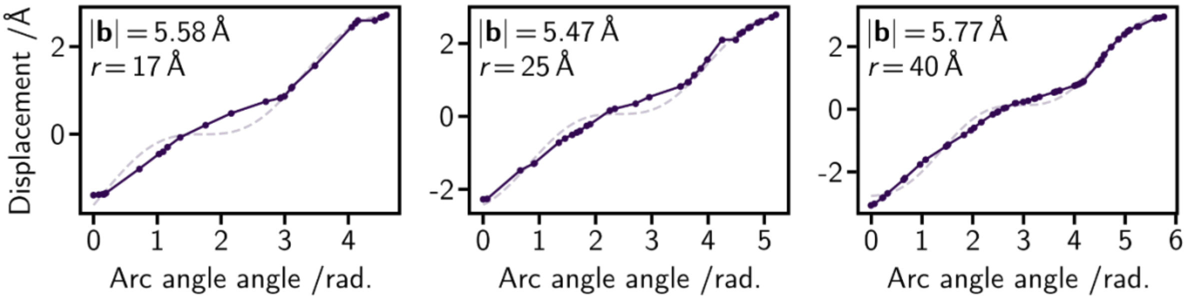

Figure S19: Burgers vector calculation for crystal in Figure 4c and d of the main text, dislocation 3: Atomic displacements as a function of arc angle as we circle the dislocation core at three different radii. Dashed lines: fit to data of function for atomic displacement, u, given in the main text. Average Burgers vector magnitude is 5.61Å.

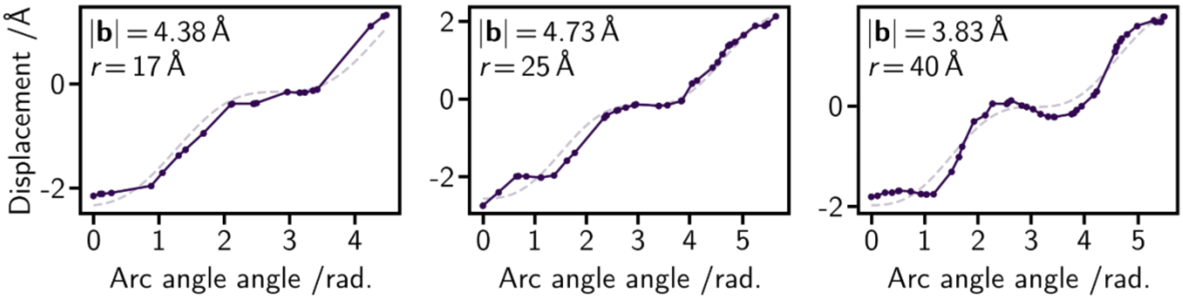

Figure S20: Burgers vector calculation for crystal in Figure 4c and d of the main text, dislocation 4: Atomic displacements as a function of arc angle as we circle the dislocation core at three different radii. Dashed lines: fit to data of function for atomic displacement, u, given in the main text. Average Burgers vector magnitude is 4.31Å. This is the dislocation with a Burgers vector $\simeq d_{110}$.

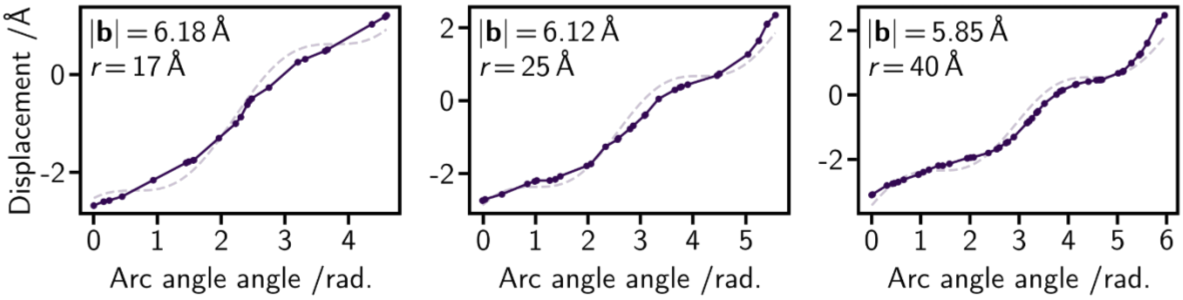

Figure S21: Burgers vector calculation for crystal in Figure 4c and d of the main text, dislocation 5: Atomic displacements as a function of arc angle as we circle the dislocation core at three different radii. Dashed lines: fit to data of function for atomic displacement, u, given in the main text. Average Burgers vector magnitude is 6.05Å.

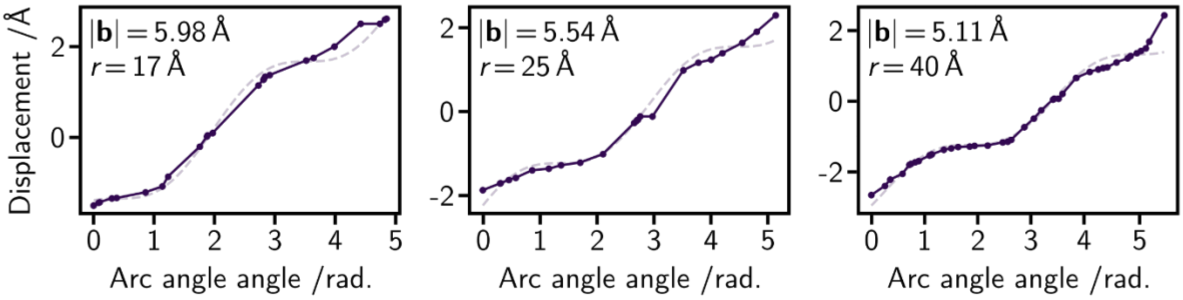

Figure S22: Burgers vector calculation for crystal in Figure 4c and d of the main text, dislocation 6: Atomic displacements as a function of arc angle as we circle the dislocation core at three different radii. Dashed lines: fit to data of function for atomic displacement, u, given in the main text. Average Burgers vector magnitude is 5.54Å.

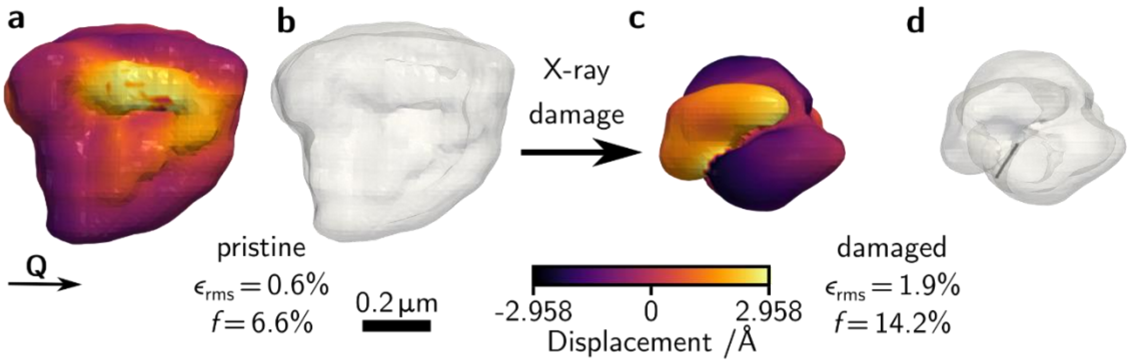

Figure S23: Additional example of X-ray induced damage and dislocation formation: Electron density reconstructions a crystal from its first BCDI scan (**a**, **b**), and from a second scan (**c**, **d**). Reconstructions are shown coloured according to the size of the atomic displacement along the direction of the scattering vector (**a**, **c**), and partially transparent in solid grey (**b**, **d**). Dislocations are shown as black lines. Exposure to X-rays damages the crystals, causing dislocation formation and increased strain (more dramatic changes in atomic displacement vector) as well as reduced crystallite volume. The scale bar and scattering vector apply to all reconstructions. Displacement *vs.* arc angle plots for the dislocation formed and the associated Burgers vectors are shown in Figure S24. Supporting Video 4 shows additional views of these reconstructions.

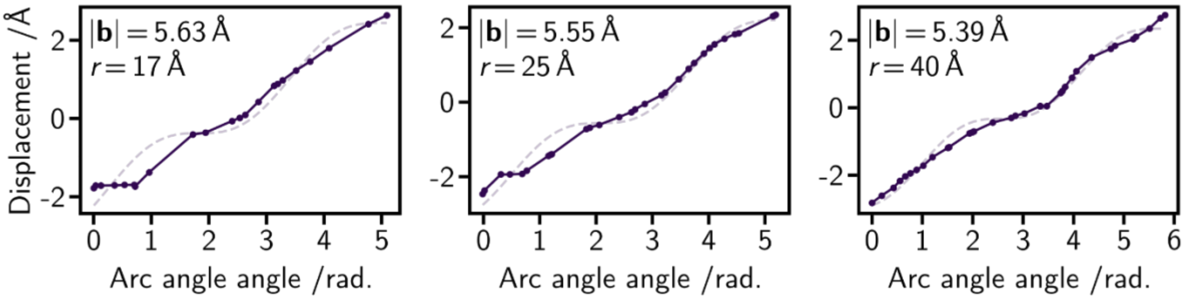

Figure S24: Burgers vector calculation for crystal in Figure S23: Atomic displacements as a function of arc angle as we circle the dislocation core at three different radii. Dashed lines: fit to data of function for atomic displacement, u, given in the main text. Average Burgers vector magnitude is 5.52Å.

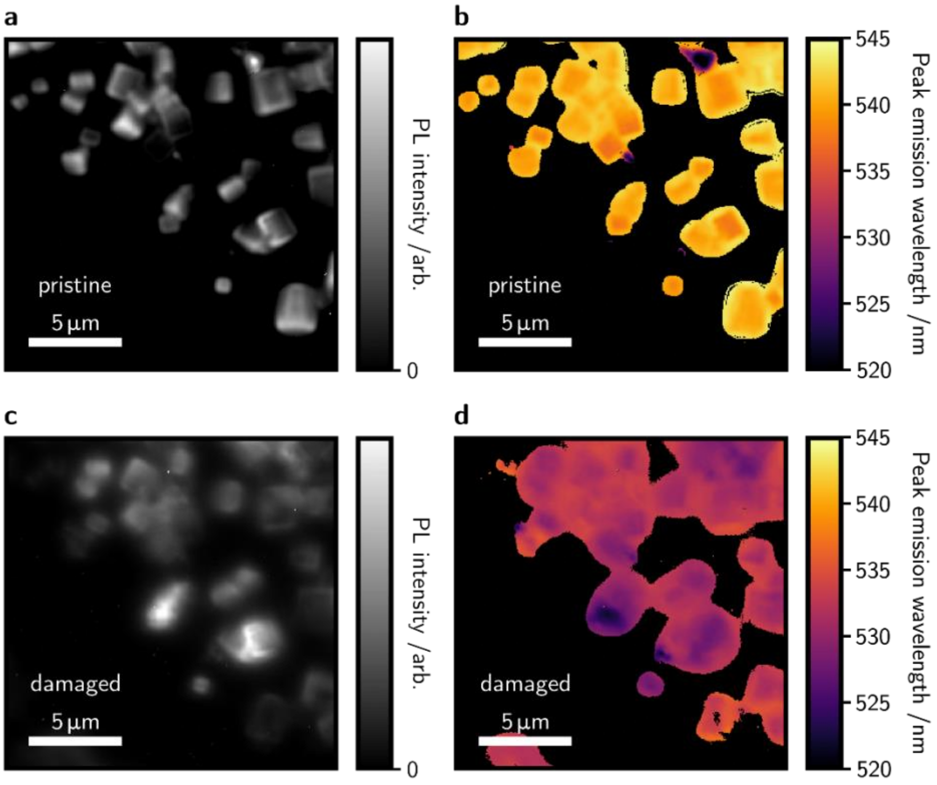

Figure S25: Photoluminescence peak emission wavelength maps for X-ray damaged crystals: a PL intensity map and **b** PL peak emission map before exposure to X-rays. **c** PL intensity map and **d** PL peak emission map after exposure to X-rays. The peak emission wavelength maps in **b** and **d** have been masked for clarity. The maps taken after exposure to X-rays are slightly out of focus due to sample drift during measurement.

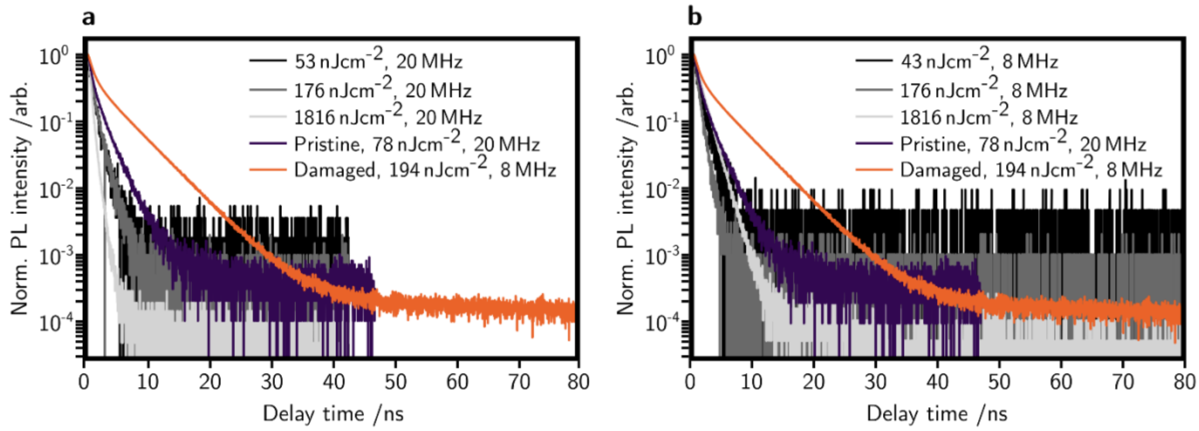

Figure S26: Fluence-dependence of PL lifetime: The time-resolved PL decay measurements for pristine (purple) $MAPbBr_3$ were collected using a fluence of 78 nJcm^{-2} and a repetition rate of 20 MHz, whereas the measurements for damaged (orange) $MAPbBr_3$ were collected using a fluence of 194 nJcm^{-2} and a repetition rate of 8MHz. To confirm that the difference in PL lifetime between these two is greater than that caused by fluence dependence, we collected time-resolved PL data on another representative sample of pristine $MAPbBr_3$ microcrystals at a range of fluences using repetition rates of **a** 20 MHz and **b** 8MHz (black, dark grey, light grey). Regardless of fluence and repetition rate, the decays for pristine $MAPbBr_3$ are similar, showing that the greater lifetime shown in Figure 4f of the main text is due to the changes induced by the X-ray beam.

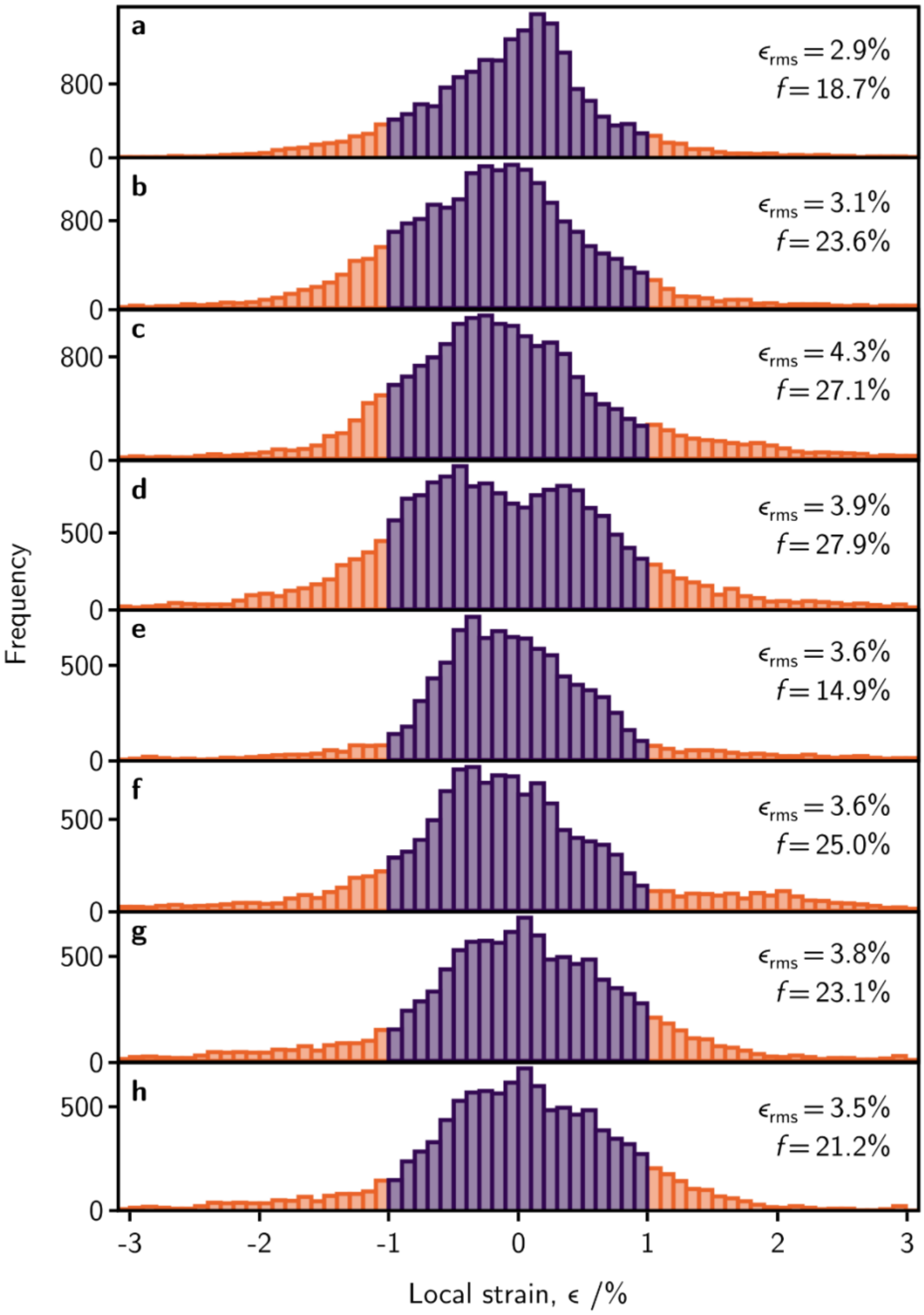

Figure S27: Local strain distributions for reconstructions of the illuminated crystal: Histograms of the local strain distribution in reconstructions shown in **a** Main text Figure 2a & Figure S2a, **b** Figure S2b, **c** Figure S2c, **d** Main text Figure 3a & Figure S2d, **e** Main text Figure 3b, **f** Main text Figure 3c, **g** Main text Figure 3d, **h** Main text Figure 3e. Values with a magnitude greater than 1% are highlighted in orange.

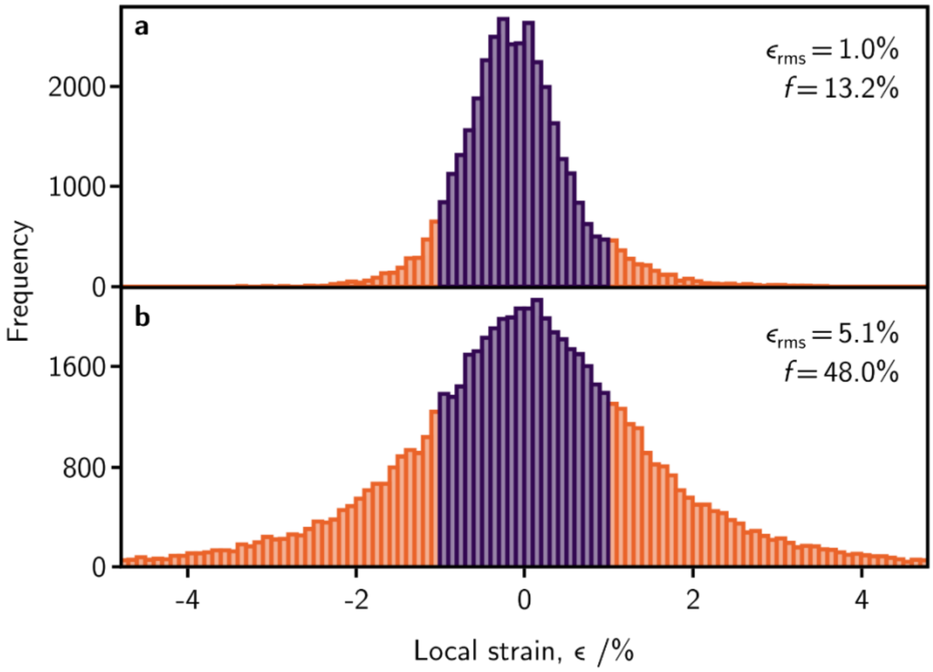

Figure S28: Local strain distributions for reconstructions of the crystal shown in Figure 4a-d of the main text: Histograms of the local strain distribution in reconstructions shown in **a** Main text Figure 4a & 4b, **b** Main text Figure 4c & 4d. Values with a magnitude greater than 1% are highlighted in orange.

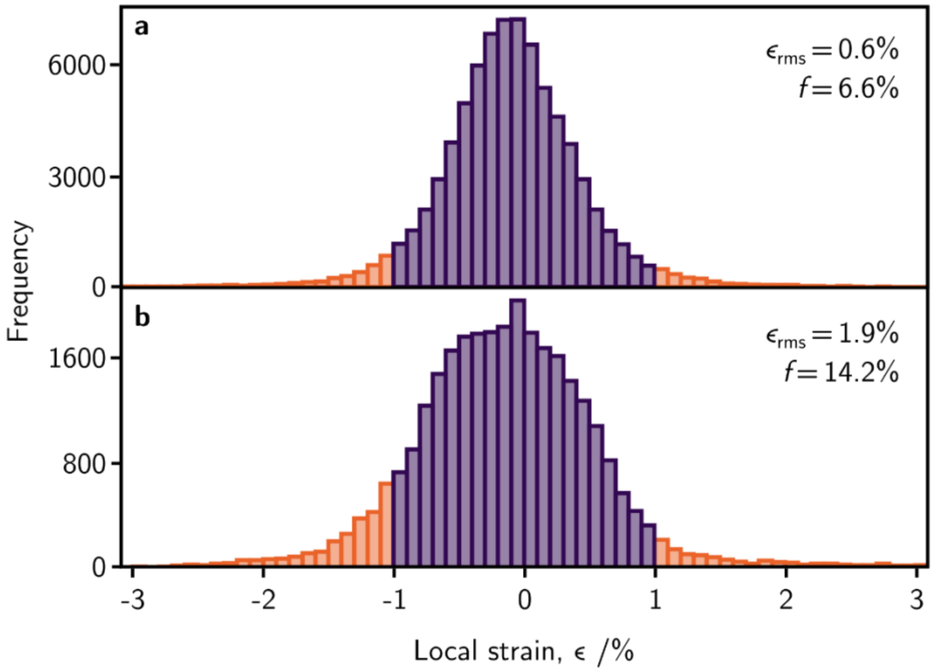

Figure S29: Local strain distributions for reconstructions of the crystal shown in Figure S23a-d: Histograms of the local strain distribution in reconstructions shown in **a** Figures S23a and S23b, **b** Figure S23c and A23d. Values with a magnitude greater than 1% are highlighted in orange.

REFERENCES:

[1] Miao, J., Ishikawa, T., Robinson, I. K., and Murnane, M. M. "Beyond crystallography: Diffractive imaging using coherent x-ray light sources", *Science* **348**, 530-535 (2015).

[2] Robinson, I. K., Da, Y., Spila, T., and Greene, J. E. "Coherent diffraction patterns of individual dislocation strain fields" *J. Phys. D: Appl. Phys.* **38**, A7-A10 (2005)

[3] Robinson, I. K. and Harder, R. "Coherent X-ray diffraction imaging of strain at the nanoscale" *Nat. Mater.* **8**, 291-298 (2009)

[4] Vartanyants, I. A. and Robinson, I. K. "Partial coherence effects on the imaging of small crystals using coherent x-ray diffraction" *J. Phys.: Condens. Matter* **47**, 10593–10611 (2001)